Influence of gravity on the frozen wave instability in immiscible liquids

D. Gligor,[1] P. Salgado Sánchez,[1] J. Porter,[1,*] and V. Shevtsova[2]

[1]*Center for Computational Simulation, Escuela Técnica Superior de Ingeniería Aeronáutica y del Espacio, Universidad Politécnica de Madrid, Plaza Cardenal Cisneros 3, 28040 Madrid, Spain*

[2]*Microgravity Research Centre, CP-165/62, Université libre de Bruxelles (ULB), avenue F. D. Roosevelt, 50, B-1050 Brussels, Belgium*

(Received 22 March 2020; accepted 30 June 2020; published 3 August 2020)

The influence of the gravity level on the frozen wave instability in finite containers of immiscible liquids is investigated numerically to shed light on the transformation from a supercritical pitchfork bifurcation in normal gravity, which produces stable finite-amplitude waves, to an apparently degenerate bifurcation in weightlessness, leading to large columnar patterns that collide with the container walls. The vibroequilibria effect grows in importance as gravity is reduced and has a symmetry-breaking effect on the bifurcation, selecting frozen waves with the heavier fluid displaced upward along the lateral walls. Three possible growth regimes are identified. With finite gravity, there is an initial gravity-capillary regime with the square-root growth predicted by weakly nonlinear theory, associated with small-amplitude waves. This is followed by a linear growth regime that is dominated by gravity and associated with larger finger-like waves. Lastly, in some cases with reduced gravity, we observe a third regime characterized by the close proximity of the frozen wave crests to the upper wall and an interval of nearly saturated wave amplitude. The defining parameters of the bifurcation diagram are measured and presented as a function of Bond number and, when possible, compared with theoretical predictions. In particular, there is excellent agreement between theory and simulations for the weakly nonlinear cubic (branching) coefficient and reasonable qualitative agreement for the threshold. Differences are attributed to finite-size effects, vibroequilibria, and viscosity.

DOI: 10.1103/PhysRevFluids.5.084001

I. INTRODUCTION

Understanding the behavior of free surfaces or interfaces and the instabilities they undergo is of basic interest in fluid dynamics, with numerous applications in biological systems and engineering. There are many well-known examples with a range of features. Gravitationally unstable configurations—or a mass of lighter fluid accelerating into a denser one after an explosion or volcanic eruption, for instance—are susceptible to the Rayleigh-Taylor instability [1], which tends to generate fingers or plumes. Temperature differences arising from an inhomogeneous heat source generally induce density gradients, which lead to buoyant (gravitational) convection [2], and surface tension gradients, which lead to thermocapillary (Bénard-Marangoni) convection [3]. The shear force resulting from a velocity difference across a fluid interface can drive a Kelvin-Helmholtz instability, which is involved in familiar phenomena such as wind-driven water waves and billow clouds. Vibrations or moving boundaries generate interfacial waves, which may be either standing or traveling, localized or distributed, depending on the direction and frequency content of the forcing.

*jeff.porter@upm.es

The dynamics resulting from these instabilities, and others, can vary considerably depending on fluid properties, the character and amplitude of the forcing mechanism, and the ratio between the system size and the length scale of the unstable mode. However, aside from small systems, gravity plays a consistently important role due to its strong preference for density stratification and the flat horizontal interfaces that characterize the static equilibrium configurations of most medium-to-large fluid masses on Earth. The familiar behavior of fluids can be dramatically altered in the absence of gravity, where surface tension favors minimum-surface configurations that are usually curved (perfectly spherical drops, for example) and contact forces can lead the fluid to fully cover any adjacent solid boundaries.

In addition to its decisive influence on equilibrium states, gravity provides a crucial restoring force for several instabilities that must be overcome at threshold (in the sense of the linear eigenvalue problem) by the driving mechanism, and which limits the subsequent growth of an unstable perturbation. As the gravity level is reduced, there is both a lowering of the threshold and more rapid growth of the excited mode. For example, small-amplitude vibrations (often called g-jitter) that would be inconsequential under normal gravity can lead to significant disturbances in microgravity environments like the International Space Station (ISS).

The Kelvin-Helmholtz instability can be triggered in a container holding two liquids of different density by periodic horizontal vibration. Starting from a perfectly flat horizontal interface in the presence of gravity, this instability arises at a critical forcing amplitude through a supercritical pitchfork bifurcation and leads initially to a quasistationary, approximately sinusoidal surface deformation referred to as a frozen wave [4–6]. The length scale of this frozen wave pattern, in sufficiently deep layers, is set by the capillary length. In microgravity, on the other hand, the threshold is drastically lowered, vanishing completely in the limit of inviscid fluids in unbounded domains. With the capillary length effectively infinite, wave number selection in microgravity is controlled by a combination of growth rate [7] and finite-size effects [8]. Moreover, the resulting patterns are not sinusoidal, or even of finite amplitude, but take the form of extended columnar structures limited only by the height of the container [9–11]. Since these columnar structures effectively rotate large portions of the interface into a nearly perpendicular orientation with respect to the forcing, this, in turn, allows Faraday waves to form when their threshold is surpassed [11–13]. The solutions resulting from this interaction are complex, with features on multiple length and time scales [11,12].

Another fluid phenomenon that is driven by vibrations and suppressed by gravity is that of vibroequilibria [4,14,15]. This effect is due to the inhomogeneous velocity field produced by the vibrations and the corresponding oscillatory pressure gradient, which induces a slow deformation of the interface toward a quasisteady equilibrium that balances forcing, gravity, surface tension, and contact energy. Faraday [16] observed this effect in his experiments on the flattening of fluid drops suspended beneath a vibrating plate. Since the vibroequilibria effect is proportional to the square of applied velocity, there is no threshold. However, it is primarily in reduced gravity environments that it becomes important for moderate or large systems (i.e., those not dominated by surface tension). In such systems, the preexisting vibroequilibria states can be expected to modify the onset of threshold instabilities like frozen waves, as well as the nature and growth of the excited modes.

In this paper we investigate the changing character of the frozen wave instability as the gravity level is varied. This dependence is especially interesting given the dramatic difference between frozen waves in normal gravity and in microgravity. In the first case, as the forcing is increased beyond the critical value, the waves grow gradually in the manner of a supercritical pitchfork bifurcation. In the second case, any forcing above the very low threshold value leads to the rapid development of large columnar patterns; no small-amplitude frozen waves are observed. The transition between these strikingly different manifestations of the same instability is examined through a series of numerical simulations using parameters relevant to both ground and microgravity experiments [12,17,18]. The transformation is characterized through the defining parameters of the bifurcation diagram including the critical forcing value, the branching (cubic nonlinear) coefficient,

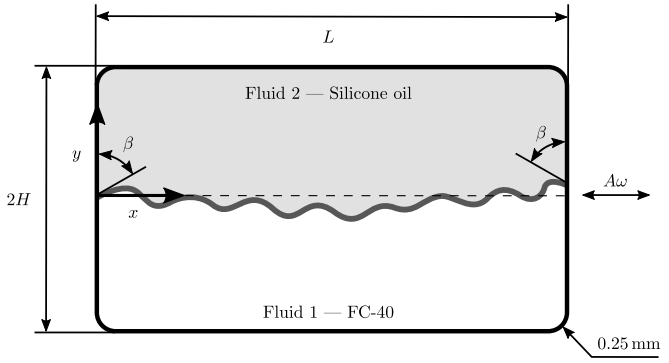

FIG. 1. Sketch illustrating the two-layer system of immiscible liquids. The rectangular container of size $L \times 2H$ is subjected to vibrations of frequency ω and amplitude A along the x axis and parallel to the initial flat interface (dashed line).

and a symmetry-breaking parameter reflecting the magnitude of the vibroequilibria effect. These are compared to theoretical predictions when available.

The paper is organized as follows. The mathematical formulation and numerical approach are presented in Sec. II. The frozen wave instability is described for the case of strong gravity in Sec. III and for reduced gravity in Sec. IV. Finite-size effects are discussed in each case. The complete results of the numerical simulations are summarized in Sec. V with the bifurcation parameters given as a function of Bond number and compared to theory. Final conclusions are offered in Sec. VI.

II. MATHEMATICAL FORMULATION

We consider a rectangular container with interior dimensions $L \times 2H$ holding two layers of immiscible liquids, as sketched in Fig. 1. The corners of the container are rounded to more closely match the relevant experiments [12,18] and avoid numerical singularities. The system is subjected to vibrations of amplitude A and frequency $\omega = 2\pi f$ oriented along the x axis, which is also parallel to the initially flat (unperturbed) horizontal interface that separates the two liquids (dashed line in the figure). In the presence of vertical gravity, this initial configuration is stable, with the heavier fluid in the lower layer.

The dynamical response to applied vibrations is resolved using a level-set method [8,12,18,19] that follows the position of the interface via a function ϕ governed by the equation

$$\phi_t + \nabla \cdot (\mathbf{u}\phi) = \gamma \nabla \cdot \left[\varepsilon \nabla \phi - \phi(1-\phi) \frac{\nabla \phi}{|\nabla \phi|} \right]. \tag{1}$$

The tuning parameter γ is set equal to $A\omega$ in this case, ε is a small diffusive term added for numerical stability and taken to be on the order of the maximum mesh element size, and the compression flux term $\phi(1-\phi)\nabla\phi/|\nabla\phi|$ counteracts the tendency of the interface to widen from numerical diffusion. This flux term was first introduced by Olsson and Kreiss [19] and is part of the standard implementation of the level-set method in the simulation environment of COMSOL Multiphysics.

The level-set function ϕ is used to continuously define density and viscosity across both layers after introducing the smoothed Heaviside function $\mathcal{H}$,

$$\rho = \rho_1 + (\rho_2 - \rho_1)\mathcal{H}, \tag{2a}$$

$$\mu = \mu_1 + (\mu_2 - \mu_1)\mathcal{H}, \tag{2b}$$

where

$$\mathcal{H}(\widetilde{\phi}) = \begin{cases} 0, & \widetilde{\phi} < -\varepsilon, \\ \frac{1}{2} + \frac{\widetilde{\phi}}{2\varepsilon} + \frac{1}{2\pi}\sin\left(\frac{\pi\widetilde{\phi}}{\varepsilon}\right), & |\widetilde{\phi}| \leqslant \varepsilon, \\ 1, & \widetilde{\phi} > \varepsilon. \end{cases} \tag{3}$$

Here $\widetilde{\phi} = \phi - 0.5$ with the values $\phi = 0,\ 1$ corresponding, respectively, to the heavier and lighter fluids denoted by subscripts 1 and 2 in Eqs. (2). The interface is associated with the contour $\phi = \mathcal{H} = 0.5$. The use of the function $\mathcal{H}$ instead of the usual Heaviside step function improves numerical stability.

In the reference frame of the container, Eqs. (1)–(3) are solved together with the continuous formulation of the incompressible Navier-Stokes equations [20]:

$$\rho[\mathbf{u}_t + (\mathbf{u}\cdot\nabla)\mathbf{u}] = -\nabla p + \nabla(\mu\,\nabla\mathbf{u}) + \delta\,\mathbf{f}_\sigma + \rho\,\mathbf{G}(t), \tag{4a}$$

$$\nabla\cdot\mathbf{u} = 0. \tag{4b}$$

Here, the effect of interfacial tension σ is included via $\mathbf{f}_\sigma$ with

$$\mathbf{f}_\sigma = (\sigma\kappa)\mathbf{n}, \quad \kappa = \nabla\cdot\mathbf{n}, \quad \mathbf{n} = \frac{\nabla\phi}{|\nabla\phi|}, \tag{5}$$

where κ is the curvature of the interface and $\mathbf{n}$ the normal vector. The effect of interfacial tension is kept local by the parameter δ, which is defined in terms of the level-set function as

$$\delta = 6\phi(1-\phi)|\nabla\phi|. \tag{6}$$

Gravity and applied periodic forcing are included in the $\mathbf{G}(t)$ term of Eqs. (4):

$$\mathbf{G}(t) = -g\,\mathbf{j} + A\omega^2\cos\omega t\,\mathbf{i}, \tag{7}$$

where g is a steady vertical gravitational field and $\mathbf{i}$ and $\mathbf{j}$ are unit vectors along the x and y axes, respectively. Values of g are given below in terms of the usual terrestrial acceleration $g_0 = 9.81\ \mathrm{m/s^2}$.

Navier-slip boundary conditions are applied on all solid walls in order to preserve the contact angle β while permitting contact line motion, as observed in the motivating experiments [12,18]. These conditions are written as

$$\mathbf{u}\cdot\mathbf{n}_\mathbf{w} = 0, \quad \mathbf{u}\cdot[\sigma(\mathbf{n}_\mathbf{w} - \mathbf{n}\cos\beta)\delta] = 0, \tag{8}$$

where $\mathbf{n}_\mathbf{w}$ is a unit vector normal to the wall. They introduce an artificial frictional force $\mathbf{f}_v = (\rho\,\nu)/\delta_v\mathbf{u}$, where $\delta_v = \sqrt{\nu/\omega}$ is the thickness of the vibrational viscous boundary layer.

As initial conditions at $t = 0$, the liquids are assumed to be motionless with $\mathbf{u} = 0$ and to be separated by a perfectly flat interface (the dashed line in Fig. 1) with $\beta = \pi/2$. To improve numerical stability, the vibrational forcing is initiated smoothly in the manner of Eq. (3) over a 0.25 s transition time, as in Refs. [8,12,18].

The simulations of interfacial dynamics with Eqs. (1)–(8) are performed with parameters appropriate for a combination of FC-40 and 100 cSt silicone oil, as given in Table I. This choice allows a comparison with several recent parabolic flight experiments [12,18] and with the ground experiments of Jalikop and Juel [17] that used silicone oil and Galden HT135, an immiscible combination with similar physical properties. Note, however, that the viscosity of FC-40 is increased in the simulations from 2.2 to 5 cSt in order to delay the appearance of secondary Faraday modes [8,12], which can interact with and complicate the analysis of the primary frozen wave structure.

The system described by Eqs. (1)–(8) may be nondimensionalized by taking H for the unit of distance, $\rho_1 - \rho_2$ for density, and $\sqrt{(\rho_1-\rho_2)H^3/\sigma}$ for time. Behavior can then be characterized by the dimensionless forcing velocity $\mathcal{F}$ and frequency Ω:

$$\mathcal{F} = A\omega\sqrt{\frac{(\rho_1-\rho_2)H}{\sigma}}, \quad \Omega = \omega H\sqrt{\frac{(\rho_1-\rho_2)H}{\sigma}}, \tag{9}$$

TABLE I. Physical and interfacial properties of FC-40 and 100 cSt silicone oil: density ρ, kinematic viscosity ν, interfacial tension σ, and contact angle β, which has been selected to achieve an initially flat interface. According to Ref. [21], interfacial tension measurements between silicone oils and FC-40 vary between 4–7 mN/m. Due to the lack of experimental measurements for 100 cSt silicone oils and FC-40, we use the same interfacial tension value as in Refs. [8,12,18]. We also note that the real kinematic viscosity of FC-40 is 2.2 cSt but is increased here to 5 cSt in order to delay the secondary Faraday wave instability.

	ρ (kg/m^3)	ν (10^{-6} m^2/s)
FC-40	1855	5
100 cSt silicone oil	965	100
	σ (10^{-3} N/m)	β (rad)
FC-40 and silicone oil	6.021	$\pi/2$

as well as the density ratio $\widehat{\rho}$, viscosity ratio $\widehat{\nu}$, capillary number Ca, Bond number Bo, and aspect ratio Γ:

$$\widehat{\rho} = \frac{\rho_2}{\rho_1}, \quad \widehat{\nu} = \frac{\nu_2}{\nu_1}, \quad \mathrm{Ca} = \nu_1\sqrt{\frac{(\rho_1-\rho_2)}{\sigma H}}, \quad \mathrm{Bo} = \frac{(\rho_1-\rho_2)H^2}{\sigma}g, \quad \Gamma = \frac{L}{2H}. \tag{10}$$

The simulation software COMSOL Multiphysics, which includes a standard implementation of the level-set method, is used for solving the two-dimensional governing equations (1)–(8) in dimensional variables with the finite-element method. Numerical convergence was previously tested in Refs. [8,12] for a similar configuration, and we make use of those results for the selection of the mesh size and the interface thickness ε. The simulations described below are performed with a maximum element size $\mathcal{S} = (7.5/50)$ mm, while ε is set to $(3/4)\mathcal{S}$ for $g \geqslant g_0$, and reduced to $(3/5)\mathcal{S}$ in reduced gravity to avoid unstable numerical behavior. The evolution in time is implemented with a generalized-α integration scheme [22] combined with streamline [23] and crosswind [24] stabilization techniques. The maximum time step is set at $1/(10f)$, with automatic reduction as required for stability. Further details of the numerical model can be found in Refs. [8,12,18].

III. FROZEN WAVE INSTABILITY IN STRONG GRAVITY

When two layers of immiscible fluids in a gravitationally stable configuration are subjected to horizontal vibrations, an initially flat interface becomes unstable to frozen waves only above a certain threshold. An expression for the critical forcing velocity $v = A\omega$ and its dependence on the perturbation wave number k was derived by Lyubimov and Cherepanov [5] in the limiting case of an infinitely long container with inviscid fluids of equal heights H, densities ρ_1 and $\rho_2 < \rho_1$, and interfacial tension σ:

$$v^2 = \frac{(\rho_1+\rho_2)^3}{2\,\rho_1\rho_2(\rho_1-\rho_2)^2}\left[\sigma k + \frac{(\rho_1-\rho_2)g}{k}\right]\tanh(kH), \tag{11}$$

which, in dimensionless form, becomes

$$\mathcal{F}^2 = \frac{(1+\widehat{\rho}\,)^3}{2\,\widehat{\rho}(1-\widehat{\rho})}\left[kH + \frac{\mathrm{Bo}}{kH}\right]\tanh(kH). \tag{12}$$

For deep layers with $kH \gg 1$, Eq. (11) implies that the wavelength of the first unstable mode is set by the capillary length,

$$\lambda_c = 2\pi\sqrt{\frac{\sigma}{(\rho_1-\rho_2)g}}, \tag{13}$$

and that its threshold v_c is given by

$$v_c^2 = \frac{(\rho_1+\rho_2)^3}{\rho_1\rho_2(\rho_1-\rho_2)}\sqrt{\frac{\sigma g}{\rho_1-\rho_2}}. \tag{14}$$

These predictions were critically examined by Talib *et al.* [6], who considered the effect of viscosity both experimentally and theoretically. It was found that the inviscid theory consistently underestimates the threshold for liquids of similar viscosity, while generally overestimating it for layers with a high viscosity contrast.

Lyubimov and Cherepanov [5] also derived an expression for the (peak-to-peak) amplitude Δh of the frozen wave pattern (see also Ref. [25]) from a weakly nonlinear analysis:

$$\Delta h^2 = \frac{16\rho_1(\rho_1+\rho_2)}{\rho_2\left(42\rho_1\rho_2-11\rho_1^2-11\rho_2^2\right)}\sqrt{\frac{\sigma(\rho_1-\rho_2)}{g^3}}\left(v^2-v_c^2\right), \tag{15}$$

or, in dimensionless form,

$$\left(\frac{\Delta h}{H}\right)^2 = \frac{16(1-\widehat{\rho}^{\,2})\mathrm{Bo}^{-3/2}}{\widehat{\rho}\,(42\,\widehat{\rho}-11-11\,\widehat{\rho}^{\,2})}\left(\mathcal{F}^2-\mathcal{F}_c^2\right), \tag{16}$$

where the subscript c indicates the critical value. It follows from Eq. (15) that for $\widehat{\rho}=\rho_2/\rho_1 > 0.2829$, which holds for most experimentally practical combinations of liquids, the instability appears via a supercritical pitchfork bifurcation. The supercritical nature of the instability was confirmed experimentally by Jalikop and Juel [17] using a pair of liquids with density contrast $\widehat{\rho}\simeq 0.548$. However, it was also observed that the square-root dependence of amplitude Δh on the distance above onset predicted by Eq. (15) changes at larger forcing values to a nearly linear one. This transition is accompanied by a change in the shape of the frozen waves, which grow from small sinusoidal waves to larger finger-like deformations.

In the remainder of this section, we analyze the frozen wave instability in finite-size containers under strong gravity. First, the behavior of the interface in terrestrial conditions at different applied forcing values is described and bifurcation diagrams showing $\Delta h(v)$ are constructed. Following this, the effects of hypergravity and finite container size, which were apparent in the experiments of Salgado Sánchez *et al.* [12], are discussed.

A. Dependence on applied forcing

Figure 2 shows the temporal evolution of the frozen wave instability with normal gravity ($g=g_0$, $\mathrm{Bo}=81.57$) in a $L\times 2H = 30\times 15$ mm container ($\Gamma=2$). The four series of snapshots use the same excitation frequency of $f=55$ Hz while the amplitude A varies in (a)–(d) from 1.1 to 1.67 mm to reach $v=0.380$, 0.432, 0.546, and 0.577 m/s, corresponding to dimensionless forcing values $\mathcal{F}=12.65$, 14.38, 15.19, and 19.22, respectively. Note that these forcing amplitudes satisfy $A\ll H$, as required for a valid comparison with linear theory [5]. They are also below the threshold for secondary Faraday waves [12].

The interface and mean velocity field are both obtained by averaging over one excitation period and are shown together during the transient growth of the pattern; in the final steady state the mean velocity is negligible and is not shown. This filters out the harmonic motion that is always present near the sidewalls due to surface waves, the evanescent oscillatory bulk flow [26,27], and the associated motion of the contact point. It can be seen from the figure that these harmonic modes do interact nonlinearly, leaving a visible bump near the sidewalls even after averaging over time. Although not often observed with the parameters used here, subharmonic waves may also be present. Neither harmonic nor subharmonic waves are investigated in this work, but we note that they are expected to play an increasingly important role with lower viscosity liquids. As shown by Salgado Sánchez *et al.* [28], the interaction of subharmonic waves from opposing lateral walls can lead to a range of complex dynamics. This interaction may even drive sloshing modes (particularly in reduced

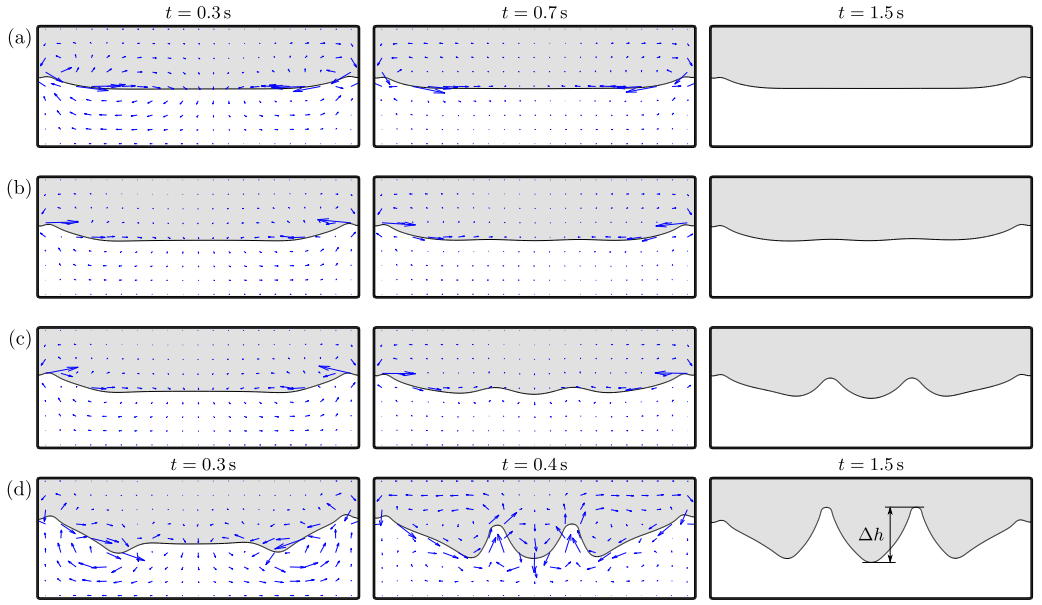

FIG. 2. Time evolution (averaged over one excitation period) of the interface and mean velocity field in a container of size $L \times 2H = 30 \times 15$ mm ($\Gamma = 2$) under normal gravity ($g = g_0$, Bo = 81.57) with different forcing amplitudes: (a) $v = 0.380$ m/s, (b) 0.432 m/s, (c) 0.456 m/s, and (d) 0.577 m/s, which correspond to $\mathcal{F}$ values of 12.65, 14.38, 15.19, and 19.22, respectively. The forcing frequency is fixed at $f = 55$ Hz while the amplitude A is increased (1.1, 1.25, 1.32, and 1.67 mm). The critical forcing is $v_c = 0.429$ m/s ($\mathcal{F}_c = 14.25$) as shown in Sec. III B. The velocity field during the transient portion of the simulation is shown with scaled arrows (scale differs between snapshots). The selected time of the intermediate snapshot in (d) is less than that of (a)–(c) due to the more rapid growth of that pattern. The final pattern in (d) also illustrates how the amplitude Δh is measured from the contour $\phi = 0.5$.

gravity) that destabilize the underlying state [29]. For some fluids and forcing parameters, the onset and development of frozen waves will be affected much more by harmonic and subharmonic surface waves than it is here.

The interface in Fig. 2 exhibits different dynamics depending on whether the applied forcing is below or above the frozen wave threshold (found in Sec. III B to be $v_c = 0.429$ m/s, or $\mathcal{F}_c = 14.25$). Below this value, as in Fig. 2(a), gravity maintains a nearly flat interface across the interior portion of the container. There is, however, an evident upward movement of the contact points along the lateral walls, as expected from the theory of vibroequilibria [14,29–32]. The vibroequilibria effect is proportional to the square of the induced vibrational velocity and is most prominent near the sides, where this inhomogeneous velocity field is strongest. It is observed across all finite applied forcing values since, unlike the frozen wave instability, it has no threshold.

When the applied forcing is just above the frozen wave threshold, two small-amplitude waves appear along the interior (flat) portion of the interface, as shown in Fig. 2(b) at $t = 1.5$ s. With further increase in forcing, these waves grow steadily in amplitude, as illustrated in Fig. 2(c), and their profile begins to take on features of an inverted trochoid. These relatively small-amplitude waves reflect the restoring forces of both gravity and interfacial tension and are in good agreement with the results of Ref. [17]. We note that the frozen wave pattern develops over the interior portion of the interface and is inhibited near the lateral walls where the vibroequilibria effect is strongest. If the cell is vibrated with still larger amplitude, as in Fig. 2(d), the tips of the inverted trochoid grow into longer finger-like protrusions, also in agreement with the experiments of Jalikop and Juel [17]. This is discussed in more detail below.

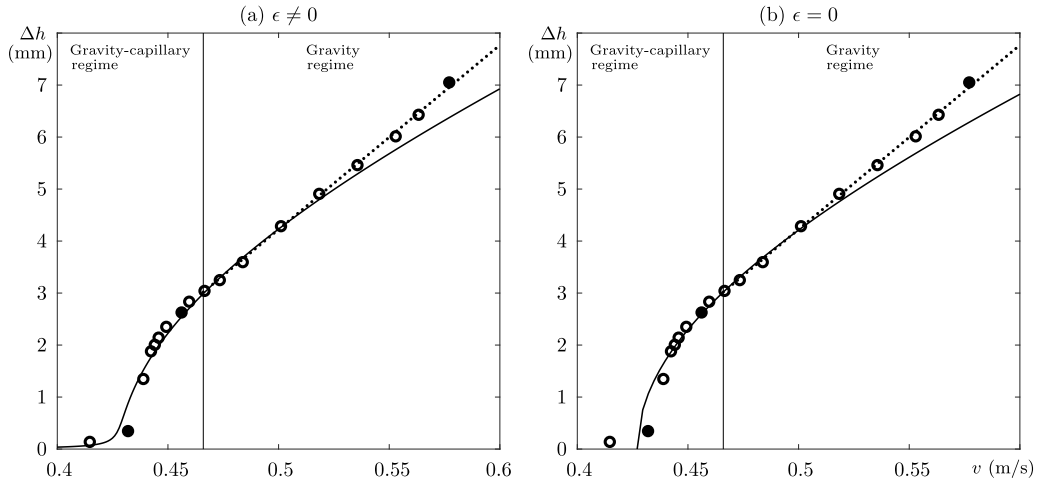

FIG. 3. Bifurcation diagram showing the trough-to-crest amplitude Δh of the frozen wave patterns versus the vibrational velocity v for $g = g_0$ in a container of size $L \times 2H = 30 \times 15$ mm. The numerically obtained points are fitted to (a) the perturbed pitchfork bifurcation of Eq. (17) or (b) the square-root dependence of Eq. (15), both shown as solid curves, and to the linear function (19), shown with a dotted line. These fits correspond to the two regimes identified by Jalikop and Juel [17], with the transition between them marked by a vertical line. The three solid markers correspond, in order of increasing v, to the snapshots of Figs. 2(b)–2(d).

In keeping with the predicted supercritical bifurcation of Eq. (15), Fig. 2 shows the continuous increase of wave amplitude with applied forcing. We take an approach similar to that of Ref. [17] in the analysis of these patterns and construct bifurcation diagrams from the measured wave amplitude.

B. Bifurcation diagram

The final (asymptotic) trough-to-crest amplitude Δh of the frozen wave pattern is measured in the manner sketched in Fig. 2(d) and bifurcation diagrams are constructed from its dependence on applied vibrational velocity v, as in Fig. 3. This figure reveals two distinct regimes, the first associated with the initial square root dependence, $\Delta h \propto \sqrt{v^2 - v_c^2}$, and the second with an approximately linear relationship, $\Delta h - \Delta h^* \propto v - v^*$, where the asterisk denotes the transition value. These regimes may be associated, as discussed below in Sec. III B 2, with a different balance between the vibrational forcing and the restoring forces of gravity and interfacial tension.

1. Character of the instability

Figure 3(a) shows that the frozen wave instability appears via a perturbed (asymmetric) supercritical pitchfork bifurcation [33]. Although we do not directly test for hysteresis by gradually lowering the forcing—simulations are always begun from rest using the smoothed Heaviside function $\mathcal{H}$ to initiate vibrations—the supercritical nature of the pitchfork bifurcation is evident from the bifurcation diagram. It is also consistent with the ideal linear theory for this density ratio and with experiments [17].

The symmetry breaking (perturbation) of the pitchfork bifurcation comes mainly from the vibroequilibria effect, which is most visible near the lateral walls. While an infinitely long, flat interface that is unstable to frozen waves may evolve toward any solution on the group orbit of equivalent patterns (i.e., solutions related by translation through some fraction of a wavelength), this is no longer possible in finite containers where the presence of the container walls modifies the vibrational velocity field. It is this same inhomogeneous velocity field that drives the average reorientation of the interface described by vibroequilibria theory. Since the effect induces the heavier

TABLE II. Parameters characterizing the bifurcation diagrams obtained at different gravity levels: symmetry-breaking parameter ϵ, critical vibrational velocity v_c, transition point v^*, width of square-root regime $v_c - v^*$, branching coefficient K, and linear fitting slope $\mathcal{M}$. Values are obtained from a least-squares fit of the data to Eq. (17), in one case with $\epsilon = 0$, and to Eq. (19).

Gravity level (units of g_0)	ϵ (10^{-9} m^3)	v_c (m/s)	v^* (m/s)	$v^* - v_c$ (m/s)	K (10^{-3} s)	$\mathcal{M}$ (10^{-3} s)
1	0	0.427	0.466	0.039	16.19	35.43
1	0.298	0.429	0.466	0.037	16.39	35.43
2	0	0.529	0.587	0.058	10.17	20.32
2	5×10^{-12}	0.530	0.587	0.057	10.16	20.32
0.5	0	0.345	0.374	0.029	26.17	67.38
0.5	0.750	0.347	0.374	0.027	26.86	67.38

fluid to climb up the lateral walls [29,30], it acts to promote the compatible frozen wave solution and suppress the others. Put another way, in the presence of the vibroequilibria effect, one cannot obtain an equivalent frozen wave pattern by inverting the crests and troughs, even at small amplitude. Due to this symmetry-breaking effect, the selected branch of the perturbed supercritical pitchfork bifurcation does not truly appear at a critical value but, instead, grows smoothly as the forcing is varied, as observed in Fig. 3(a).

The two regimes of amplitude growth distinguished by Jalikop and Juel [17] are also apparent in Fig. 3. Data points in the first regime are fitted, for comparison, to both an ideal and a perturbed pitchfork branching equation, while those in the second regime are fitted to a linear function. The branching equation for a perturbed supercritical pitchfork bifurcation can be written

$$\Delta h^3 - K^2\left(v^2 - v_c^2\right)\Delta h + \epsilon = 0, \tag{17}$$

which, with the corresponding value of K^2, reduces to Eq. (15) when $\epsilon = 0$. With $g = g_0$, the values of v_c and K obtained from least-squares fits with $\epsilon = 0$ and $\epsilon \neq 0$ are similar:

$$v_c = 0.427 \text{ m/s}, \quad \text{for } \epsilon = 0, \tag{18a}$$

$$v_c = 0.429 \text{ m/s}, \quad \text{for } \epsilon \neq 0. \tag{18b}$$

In the latter case, the fitting yields $\epsilon = 0.298 \times 10^{-9}$.

The linear regime is characterized by a least-squares fit to the linear function,

$$\Delta h - \Delta h^* = \mathcal{M}(v - v^*), \tag{19}$$

which provides the slope $\mathcal{M}$ as well as the forcing v^* and amplitude Δh^* characterizing the transition. The points included in each fitting are selected from the root mean square error (RMSE) and the associated R^2 value. Successive data points, ordered by increasing v, are included in the first regime rather than the second only if the resulting RMSE decreases or the R^2 value increases. The results of these fittings for $g = g_0$ are summarized in the first two rows of Table II.

2. Curvature and energy balance

Following Jalikop and Juel [17], we quantify the curvature of the final patterns obtained by simulations. Figure 4(a) shows the curvature r_k measured at the crests of frozen wave patterns with $g = g_0$ as a function of vibrational velocity v. This radius of curvature is measured by averaging the $\phi = 0.5$ contour of the level-set function over one forcing period. The averaged contour is then linearly interpolated to obtain a representation $y = f(x)$ from which first and second derivatives, f'

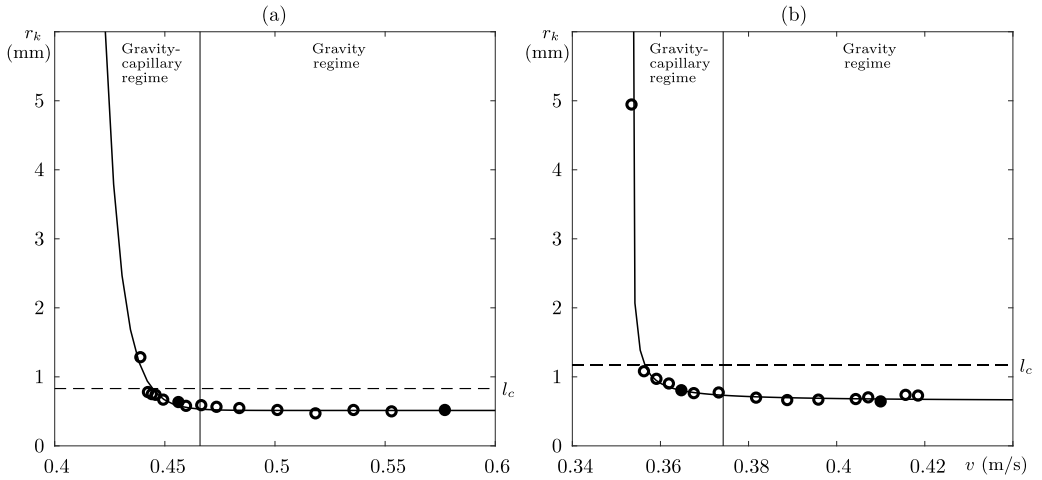

FIG. 4. Radius of curvature r_k at the wave crests as a function of the applied velocity v for (a) $g = g_0$ and (b) $g = 0.5g_0$. Data points are fitted with a solid curve for visual reference. Asymptotic behavior is seen at large v when r_k is comparable to the capillary length (shown with a dashed line) given by Eq. (21). The two solid markers in (a) correspond to the snapshots of Figs. 2(c) and 2(d) while those in (b) correspond to the snapshots of Figs. 6(c) and 6(d), shown below.

and f'', are calculated using second-order Lagrange polynomials. The radius of curvature is

$$r_k = \frac{[1 + (f')^2]^{\frac{3}{2}}}{|f''|}. \tag{20}$$

Figure 4(a) clearly shows how this curvature r_k decreases toward a value commensurate with the capillary length (shown by a dashed line):

$$l_c = \frac{\lambda_c}{2\pi} = \sqrt{\frac{\sigma}{(\rho_1 - \rho_2)g}}. \tag{21}$$

This asymptotic behavior corresponds to the transition from a trochoid-like shape to a finger-like shape; compare panels (c) and (d) of Fig. 2. The transition occurs near the forcing value v^* (shown by a solid vertical line) defined by the change from square root to linear growth of the amplitude Δh (see Fig. 3). The limiting behavior reflects the fact that, beyond v^*, the shape of the frozen wave crests does not vary significantly with amplitude. This is in agreement with the experiments of Jalikop and Juel [17], which exhibited the same trend. The presence of these two different supercritical regimes with their corresponding frozen wave shapes can be related to the balance between forcing, gravity, and interfacial tension that holds in each case, as discussed as well in Ref. [17].

Energy balance in the gravity-capillary regime. When the frozen waves are small and sinusoidal with $k\Delta h \ll 1$ [see Fig. 2(b)], the gravitational and interfacial energies, E_g and E_σ, of a single frozen wave can be approximated as

$$E_g = \frac{\pi(\rho_1 - \rho_2)g}{8k}\Delta h^2, \quad E_\sigma \simeq \frac{2\pi\sigma}{k} + \frac{\pi\sigma k}{8}\Delta h^2. \tag{22}$$

The expression for E_g follows from the fact that the centroid of the positive half of a sine wave is located at a height $\pi\,\Delta h/16$ while its area is $\Delta h/k$. The expression for E_σ follows from an expansion of the elliptic integral giving the arc length of a sine wave; note that the first term is just the energy of the unperturbed flat interface.

If forcing is increased, the amplitude Δh of the frozen wave will grow until it is matched by the restoring forces of gravity and interfacial tension,

$$\frac{\partial E_g}{\partial \Delta h} = \frac{\pi(\rho_1 - \rho_2)g}{4k}\Delta h, \quad \frac{\partial E_\sigma}{\partial \Delta h} \simeq \frac{\pi\sigma k}{4}\Delta h, \tag{23}$$

which are both proportional to the amplitude Δh and are equal in the ideal case of Eq. (13) with $k = 2\pi/\lambda_c = \sqrt{(\rho_1 - \rho_2)g/\sigma}$. For frozen waves near this selected wave number, both gravity and interfacial tension provide restoring forces of similar magnitude. This balance characterizes the initial supercritical regime of Fig. 3 showing an approximate square-root dependence: $\Delta h \propto \sqrt{v^2 - v_c^2}$. As the frozen wave amplitude grows, however, the curvature of the crests and troughs reaches a limiting value (see Fig. 4) and, beyond this, interfacial energy increases slower than gravitational energy, which marks the gravity-dominated regime.

Energy balance in the gravity regime. Far from threshold, when $k\Delta h \gtrsim 1$, the frozen waves develop into finger-like shapes with the tips maintaining approximately the same form (i.e., their curvature is nearly constant). As in the gravity-capillary regime, the gravitational energy of the finger-like waves is proportional to Δh^2 (coming from the product of centroid height and wave area). In contrast, the interfacial energy of these nonlinear waves is proportional to Δh (finger length):

$$E_g \simeq c_1(\rho_1 - \rho_2)g\Delta h^2, \quad E_\sigma \simeq E_{\text{tips}} + c_2\sigma\,\Delta h, \tag{24}$$

where c_1 and c_2 are approximately constant geometric factors depending on the shape and size of the tips and E_{tips} denotes their nearly constant interfacial energy. In this regime, the restoring forces can be estimated from

$$\frac{\partial E_g}{\partial \Delta h} \simeq 2c_1(\rho_1 - \rho_2)g\Delta h, \quad \frac{\partial E_\sigma}{\partial \Delta h} \simeq c_2\sigma, \tag{25}$$

which means that gravity dominates over interfacial tension for large Δh and is responsible for determining the amplitude of large finger-like frozen waves. This corresponds to the second, nearly linear regime of Fig. 3.

These basic energy arguments show how the evolution of frozen waves from small-amplitude sinusoidal profiles to nonlinear trochoid or finger-like shapes is associated with the transition from a gravity-capillary forcing balance to a gravity-dominated restoring force, which produces a noticeable change in the $\Delta h(v)$ curve. The same transition was analyzed by Jalikop and Juel [17] for layers of Galden HT135 and silicone oil of 100 or 200 cSt. We note that although the growth of the frozen wave amplitude in the nonlinear finger-like regime is dominated by gravity, interfacial tension is essential in determining the shape of the tips and limiting their radius of curvature. In the absence of (strong) interfacial tension, as in the experiments with miscible liquids of Gaponenko *et al.* [34], the frozen waves adopt a more triangular profile, which is also affected by gravity [35].

C. Effect of hypergravity

The linear results of Lyubimov and Cherepanov [5] show how the combination of gravity and interfacial tension determines both the frozen wave threshold, given by Eq. (11), and the wavelength of the emerging pattern, given by Eq. (13) for $kH \gg 1$. With an increase in gravity level, greater forcing is required to excite frozen waves and their wavelength (set by the capillary length) is reduced. Recent results from parabolic flight experiments [12] (see Sec. 6.4 of that reference) included some observations of frozen waves initiated in hypergravity, with the expected decrease in wavelength compared to the pure microgravity results.

These effects of increased gravity level are demonstrated in Fig. 5(a), which shows the bifurcation diagram for $g = 2g_0$ (Bo = 163.14) alongside the results of Fig. 3 with normal gravity. A typical frozen wave pattern is illustrated in the inset provided for the hypergravity case, showing a clear decrease in wavelength compared to the patterns of Fig. 2.

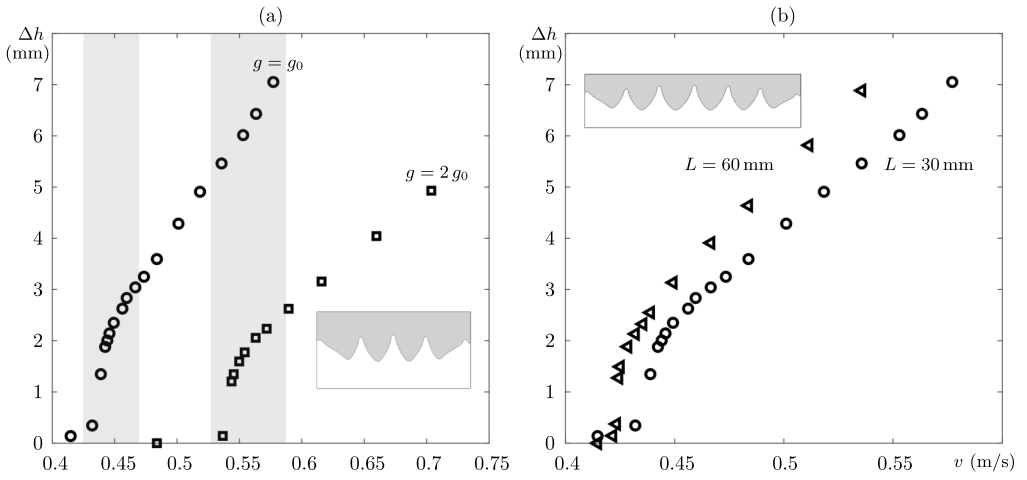

FIG. 5. (a) Bifurcation diagrams showing $\Delta h(v)$ with $g = 2g_0$ (Bo = 163.14, squares) and $g = g_0$ (Bo = 87.57, circles) in a container of size $L \times 2H = 30 \times 15$ mm ($\Gamma = 2$). The initial capillary-gravity regime of each diagram, with the interval given in Table II by $(v^* - v_c)$, is shaded. (b) Bifurcation diagrams under normal gravity, $g = g_0$, in containers of size $L \times 2H = 30 \times 15$ mm ($\Gamma = 2$, circles) and $L \times 2H = 60 \times 15$ mm ($\Gamma = 4$, triangles). The insets show representative patterns, to be compared with Fig. 2, for (a) the hypergravity case and (b) the longer container with $\Gamma = 4$.

The threshold with $g = 2g_0$ is delayed with respect to normal gravity [see Table II and Eqs. (18)]:

$$v_c|_{2g_0} = 0.529 \text{ m/s}, \quad \text{for } \epsilon = 0, \tag{26a}$$

$$v_c|_{2g_0} = 0.530 \text{ m/s}, \quad \text{for } \epsilon \neq 0. \tag{26b}$$

The relative increase in threshold is approximately 1.24 (0.529/0.427 for $\epsilon = 0$ and 0.530/0.429 for $\epsilon \neq 0$) and in reasonable agreement with the value of $2^{1/4} \simeq 1.19$ predicted by Eq. (14). The difference may be attributed to the effect of viscosity [6,36] and to the finite container size [8], the influence of which is discussed below.

D. Effect of finite container length

Figure 5(b) presents bifurcation diagrams for two different container sizes: $L \times 2H = 30 \times 15$ mm ($\Gamma = 2$, shown with circles) and $L \times 2H = 60 \times 15$ mm ($\Gamma = 4$, shown with triangles). A representative frozen wave pattern is shown in the inset for the $\Gamma = 4$ case and can be compared with Fig. 2.

Finite-size effects are expected to play a significant role whenever the number of frozen waves appearing in the container is not large. The lateral boundary conditions in that case are an important part of the wave number selection problem and can be expected, in general, to prevent frozen waves at the ideal wave number (the minimum of the neutral stability curve for an infinitely long container) from developing; this may be thought of as wave number frustration. Another, more subtle, effect is the modification of the base flow due to the boundaries. The ideal horizontal counterflow assumed by Lyubimov and Cherepanov [5] cannot hold in finite containers. Since the oscillatory flow must turn up or down as it approaches the lateral walls, this can be expected to weaken the Kelvin-Helmholtz mechanism and increase the frozen wave threshold. Consistent with the diminishing of both effects in longer containers, a slight reduction of the threshold is observed with $L = 60$ mm in Fig. 5(b). The overall shape of the bifurcation diagram is not significantly affected, however.

Finite-size effects are much more prominent in microgravity conditions, as discussed by Salgado Sánchez *et al.* [8], since the most dangerous perturbations according to Eq. (13) are longwave modes

that invariably interact with the boundaries. In hypergravity, on the other hand, the selection of a higher wave number reduces the importance of the boundaries.

IV. FROZEN WAVE INSTABILITY IN REDUCED GRAVITY

In reduced gravity conditions, the patterns that emerge from the frozen wave instability can exhibit very different behavior compared to terrestrial experiments. Equation (13) shows that in the limiting case of $g = 0$, the capillary length becomes infinitely large. Furthermore, the threshold (11) vanishes for modes with $k \to 0$ so that some type of extended frozen wave mode is expected with minimal forcing. If a larger finite forcing value is given, the length scale of the instability can be estimated by determining the fastest growing perturbation within the band of unstable wave numbers [7,37].

In addition to the contrasting features of the linear problem, the nonlinear evolution of frozen waves above onset can also differ dramatically in the absence of the (usually dominant) gravitational restoring force. Rapid growth is typically observed, with the frozen waves rearranging into large columnar structures [9,11,12] that are constrained only by the size of the container [8]. Moreover, the absence of gravity promotes the vibroequilibria effect [31], which can interact with the frozen wave instability.

Given the fact that the frozen wave instability and subsequent pattern selection process in microgravity differ so dramatically from the case of normal gravity, significant qualitative changes in the bifurcation diagram must occur as gravity (Bond number) is reduced. An analysis of the frozen wave instability under various gravity levels, including the limiting case of $g = 0$, is presented below.

A. Dependence on applied forcing

Through four series of snapshots with increasing v between 0.282 and 0.410 m/s ($\mathcal{F}$ between 9.41 and 13.65), Fig. 6 illustrates the evolution of the instability under reduced gravity conditions ($g = 0.5g_0$, Bo = 40.79) in the $L = 30$ mm container. The simulations are performed at a fixed frequency of $f = 45$ Hz with increasing amplitudes A from 1 to 1.45 mm, all satisfying $A \ll H$. The interface position is again averaged over one excitation period, as is the transient velocity field shown in the first two snapshots of each series.

As discussed in Sec. III, the interface begins to take on a different shape as the forcing increases beyond the frozen wave threshold, $v_c = 0.347$ m/s ($\mathcal{F}_c = 11.55$); the determination of this onset value is discussed in Sec. IV B. Below this threshold, as in the snapshots of Fig. 6(a), the interface slowly reorients by moving upward in the vicinity of the lateral walls, which is the behavior expected from vibroequilibria theory [29,30]. The degree of deformation is comparable to that found in the simulations of Fig. 2(a) under normal gravity, but for a vibrational velocity approximately 26% smaller. The behavior shown in Figs. 6(c) and 6(d) for $v = 0.364$ and 0.410 m/s, respectively, reveals a more pronounced vibroequilibria effect with greater displacement of the contact points than in Fig. 2(a), which was made with an intermediate value of $v = 0.380$ m/s. This magnification of the vibroequilibria effect in reduced gravity is expected.

At forcing values near the threshold of $v_c = 0.347$ m/s, small-amplitude frozen waves coexist with the underlying vibroequilibria state, as seen in Fig. 6(b). The waves first appear in the interior (flat) portion of the interface since the Kelvin-Helmholtz mechanism is generally suppressed by proximity to the lateral walls and by the curvature of the vibroequilibria solution. For the frozen wave instability, this results in a reduction of the effective container length.

Further above threshold, as in Fig. 6(c), the frozen wave amplitude grows large enough to be clearly seen above the vibroequilibria effect. This solution can be compared with that of Fig. 2(c), where the frozen wave profile is composed of two waves spanning approximately half of the container length, in contrast to the single peak that develops here for the same container geometry. This increase in wavelength under the reduced gravity of $g = 0.5g_0$ is consistent with the ideal linear

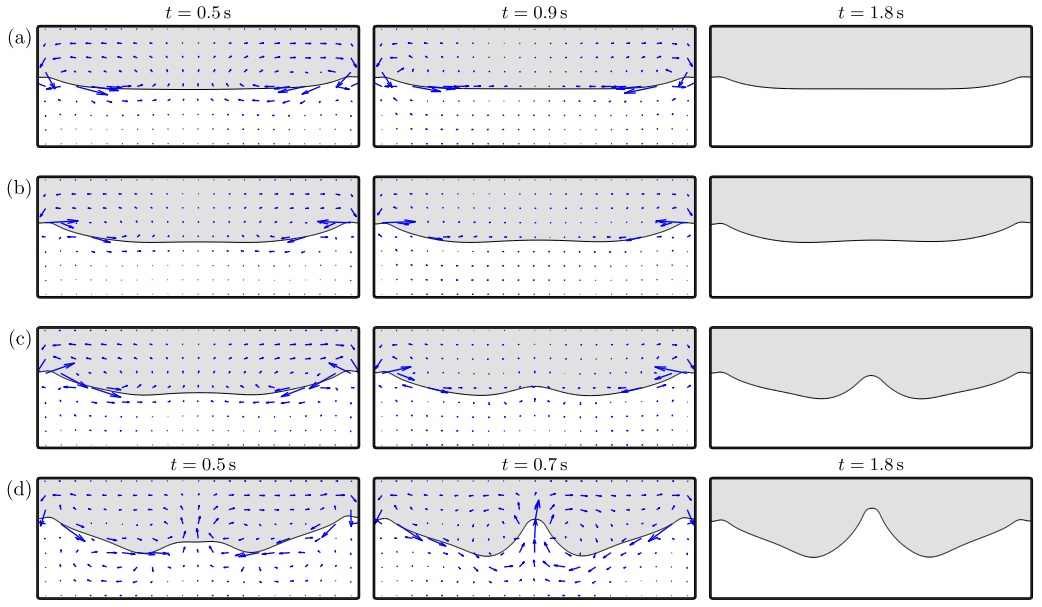

FIG. 6. Time evolution (averaged over one excitation period) of the interface and mean velocity field in a container of size $L \times 2H = 30 \times 15$ mm ($\Gamma = 2$) under reduced gravity $g = 0.5g_0$ (Bo = 40.79). Increasing vibrational forcing is applied: (a) $v = 0.282$, (b) 0.344, (c) 0.364, and (d) 0.410 m/s, corresponding to $\mathcal{F} =$ 9.41, 11.49, 12.14, and 13.65, respectively. The frequency is fixed at 45 Hz with the amplitude increased from 1 to 1.45 mm. The critical forcing is $v_c = 0.347$ m/s ($\mathcal{F}_c = 11.55$); see Sec. IV B. The velocity field during the transient portion of the simulation is shown with scaled arrows (scale differs between snapshots). The selected times of series (a)–(c) are labeled at the top while, due to more rapid growth, the intermediate snapshot in (d) is taken at 0.7 s instead of 0.9 s.

theory of Eq. (13) and with the reduction of effective container length induced by the vibroequilibria effect. The qualitative shape of the frozen wave, however, is similarly trochoid-like in both cases.

Still further above threshold, as in Fig. 6(d), the frozen wave grows in amplitude and undergoes a qualitative change in its shape, similar to the transition described in Sec. III. Figure 4(b) shows that the radius of curvature at the crests again reaches an asymptotic value, in this case larger than in Fig. 4(a) with $g = g_0$, that limits the sharpness of the finger-like tip. Once more, the asymptotic value of r_k is comparable to the capillary length, given by Eq. (21).

The mean velocity field behaves in a very similar fashion in Figs. 6 and 2. The development of a frozen wave profile is associated with a structure of large vortices that travels inward, deforming the interface. While qualitatively similar, these vortices driving the interface toward the final frozen wave state are larger here, consistent with the longer wavelength (a single frozen wave peak in the final pattern).

B. Bifurcation diagram

As in Sec. III B, we obtain the bifurcation diagram characterizing the frozen wave instability with $g = 0.5g_0$ by measuring the trough-to-crest distance Δh. These values are shown in Fig. 7 (using solid circles) as a function of applied velocity v. Three distinct regions can be identified from that figure: the initial capillary-gravity (square-root) regime, the subsequent gravity regime, and for even higher forcing, a new regime dominated by the effect of the finite container depth. The data points corresponding to the solutions of Figs. 6(b)–6(d) are distinguished by open circles, as are the

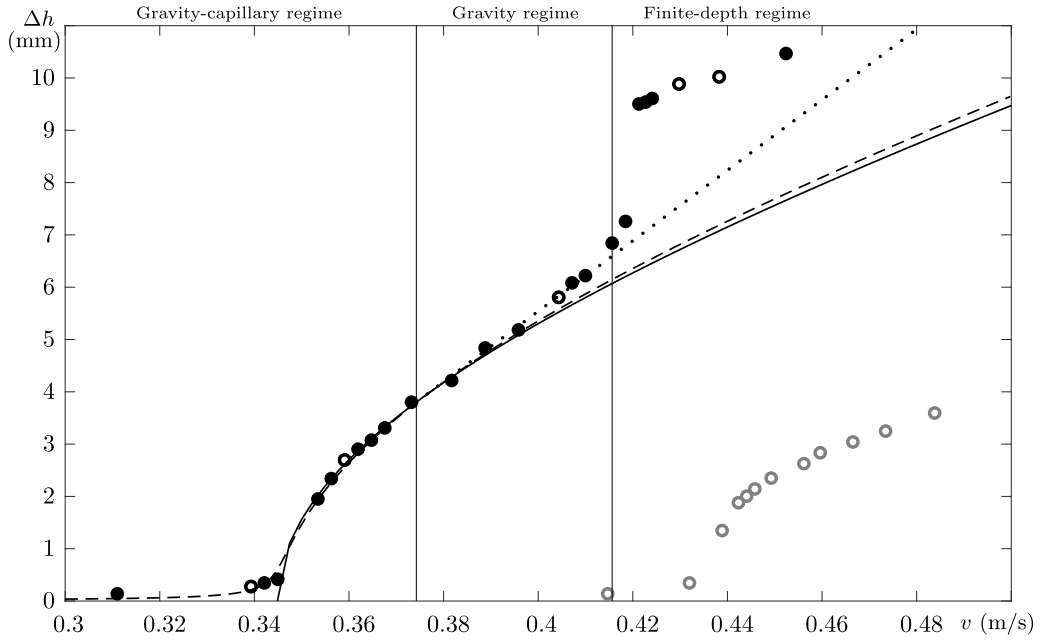

FIG. 7. Bifurcation diagram showing the trough-to-crest distance Δh of the frozen wave patterns versus vibrational velocity v for $g = 0.5g_0$ in a container of size $L \times 2H = 30 \times 15$ mm. The measurements in the gravity-capillary regime are fitted to the branching equation (17) of a perturbed pitchfork (dashed curve) and of the unperturbed ($\epsilon = 0$) case (solid curve). The gravity regime is fitted to the linear function (19) (dotted curve). The transitions between different regimes (labeled above) are highlighted by vertical lines, including the new finite-depth regime where the crest approaches the upper boundary. The five points distinguished by open black circles correspond, in order of increasing v, to the snapshots of Figs. 6(b)–6(d) and Figs. 8(a) and 8(b). The diagram of Fig. 3 for normal gravity is included for comparison (open gray circles).

two simulations shown later in Fig. 8. For ease of comparison, the bifurcation diagram with normal gravity from Fig. 3 is included using open gray circles.

Figure 7 reconfirms that the frozen wave instability occurs via a perturbed (asymmetric) supercritical pitchfork [33]. Recall that, in the ideal linear theory, the supercritical nature depends only on the density ratio $\widehat{\rho}$, while the asymmetric perturbation is mainly due to the vibroequilibria effect. As in Sec. III B, the numerical points near onset are fitted to the branching equation (17) of a pitchfork bifurcation both in the ideal ($\epsilon = 0$) and perturbed ($\epsilon \neq 0$) cases, which yields the critical amplitudes

$$v_c|_{0.5g_0} = 0.345 \text{ m/s}, \quad \text{for} \quad \epsilon = 0, \tag{27a}$$

$$v_c\big|_{0.5g_0} = 0.347 \text{ m/s}, \quad \text{for} \quad \epsilon \neq 0, \tag{27b}$$

and the coefficient K. While the frozen wave threshold increases in the hypergravity case of Sec. III C, it is reduced with lower gravity levels, by a factor of approximately 0.81 for $g = 0.5g_0$, which is consistent with the prediction of $2^{-1/4} \simeq 0.84$ from Eq. (14).

For higher values of vibrational velocity, the data are fitted to Eq. (19) to obtain the transition value v^* and the linear growth rate $\mathcal{M}$. These fits use the same RMSE and R^2 error criteria as Sec. III B, and provide the values listed in Table II. The coefficient K of the capillary-gravity regime is larger than with normal gravity, reflecting the more rapid growth of frozen waves with a reduced gravitational restoring force. This is also evident from direct comparison of the bifurcation diagrams for $g = 0.5g_0$ and $g = g_0$ (gray markers) in Fig. 7.

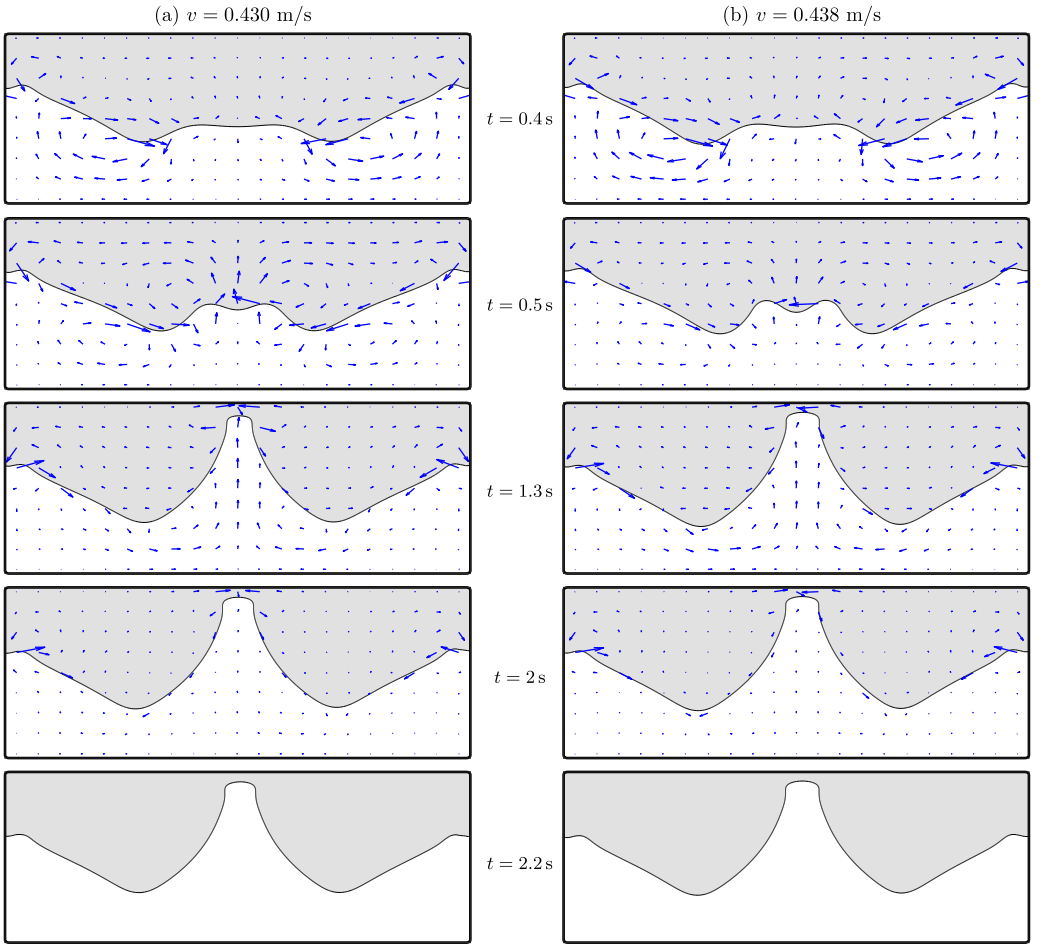

FIG. 8. Time evolution (averaged over one excitation period) of the interface and mean velocity field illustrating the frozen wave instability for $g = 0.5g_0$ in the finite-depth regime in a container of size $L \times 2H = 30 \times 15$ mm vibrated at $f = 45$ Hz and amplitudes (a) $A = 1.52$ mm ($v = 0.430$ m/s, $\mathcal{F} = 14.31$), (b) $A = 1.55$ mm ($v = 0.438$ m/s, $\mathcal{F} = 14.59$). The time of the snapshot is labeled between the columns. The velocity field is shown using scaled arrows (scale differs between snapshots). The Δh values obtained from these two simulations are marked with open circles in Fig. 7.

The more rapid growth of the frozen waves extends as well, if not more so, into the gravity regime—less forcing is needed to achieve a given increase in amplitude compared to the normal gravity case. The approximately linear dependence, however, does not hold beyond $v \simeq 0.416$ m/s. At this point, there is an abrupt increase in Δh followed by a kind of saturation with $\Delta h \sim H$. This transition is explained by the finite depth of the container, which affects and limits the growth of large-amplitude waves, as described in the following section.

1. Effect of finite container depth

Figure 8 shows the evolution of the frozen wave pattern in the finite-depth regime for 45 Hz forcing with amplitudes of $v = 0.430$ m/s ($\mathcal{F} = 14.31$) and $v = 0.438$ m/s ($\mathcal{F} = 14.59$). The initial evolution is broadly similar in both cases to that previously illustrated in Fig. 6(d). Vortices appear near the lateral walls accompanying the motion of the contact points and the progression

of the deformations (frozen waves) toward the interior of the container. As observed in Figs. 2 and 6, the wave profile is not reflection symmetric about the horizontal midline. In addition to vibroequilibria effects, the troughs are broader and shallower than the crest(s). If the forcing is strong enough, the central crest reaches the vicinity of the upper wall while the troughs remain a certain distance from the lower boundary (see the snapshots at $t = 1.3$ and 2 s). The increase in forcing from 0.430 to 0.438 m/s does not noticeably affect the vertical location of the crest but does broaden it slightly, while the troughs grow a bit deeper and more separated.

For the forcing values of Fig. 8, the tip of the finger-like wave flattens and avoids a true collision with the upper wall. Prior to this, the maximum curvature of the tip takes an asymptotic value near the capillary length, but there can be a significant increase in curvature in the finite-depth regime at the "corners" of the flattened tip. This suggests that interfacial energy is locally balanced here by strong fluid motion (through the narrow gap above the tip) rather than gravity. At sufficient forcing amplitude, the interface will collide with the upper boundary and split to create a columnar shape, as commonly observed following the frozen wave instability in weightlessness [9,11,12]. Behavior similar to that of Fig. 8 was described in Ref. [8] for patterns resulting from the frozen wave instability in microgravity in finite containers.

2. Mode competition

As described in Salgado Sánchez *et al.* [8], the container dimensions play a crucial role in the pattern selection process in reduced gravity. The finite length L permits only certain wave numbers and suppresses the others. Transitions between distinct modes occur as the forcing increases since the wave number of the fastest growing perturbation generally increases with forcing [7]. For the vibrational amplitudes of Fig. 6, the fastest growing perturbation is close to a mode with two large troughs and a single crest in the middle of the container, which is eventually selected as the final pattern. Modes of higher wave number can be observed, over finite intervals, at higher forcing.

The pattern selection process in this system is complicated by the vibroequilibria effect, as mentioned Sec. III. The heightened curvature of the average interface near the lateral walls, in addition to shifting the threshold, can be assumed to reduce the effective length of the container that is susceptible to Kelvin-Helmholtz instability, thereby directly affecting wave number selection. The vibroequilibria effect also promotes those solutions having the heavier fluid displaced upward near both lateral walls. In general, the complicated interaction between vibroequilibria and frozen waves continues into the nonlinear regime and can be expected to influence mode interactions like that seen in Fig. 8.

For convenience, we define the pattern wave number $\mathcal{K}$ as the number of troughs observed in the frozen wave profile. For example, the final patterns shown in Figs. 2(d) and 6(d) correspond to the $\mathcal{K} = 3$ and $\mathcal{K} = 2$ modes, respectively. The snapshots of Fig. 8 at $t = 0.5$ s indicate that the initially dominant frozen wave perturbation is close to the $\mathcal{K} = 3$ mode but, by $t = 1.3$ s, the small-amplitude wave in the center of the container is absorbed into the faster-growing $\mathcal{K} = 2$ mode.

Vibrational forcing was increased in order to encourage the $\mathcal{K} = 3$ mode in Fig. 9, which shows snapshots of the interface development in the same container with $g = 0.5g_0$ vibrated at $f = 45$ Hz, but with $A = 1.6$ mm ($v = 0.452$ m/s). Up to $t \simeq 0.5$ s, the average interface is almost left-right symmetric, with both crests growing at similar rates. With more time, however, the solution becomes increasingly asymmetric as the crest on the right, but not the left, grows to reach the vicinity of the upper wall by $t \simeq 1.5$ s. The amplitude of the left crest then diminishes and disappears, completing a transition to the $\mathcal{K} = 2$ mode by $t \simeq 2.5$ s. It requires forcing exceeding $v = 0.452$ m/s to fully stabilize the $\mathcal{K} = 3$ mode.

C. Microgravity

As demonstrated above, a reduction in the gravity level has a clear effect on the frozen wave instability, lowering its threshold and allowing more rapid growth of large-amplitude patterns.

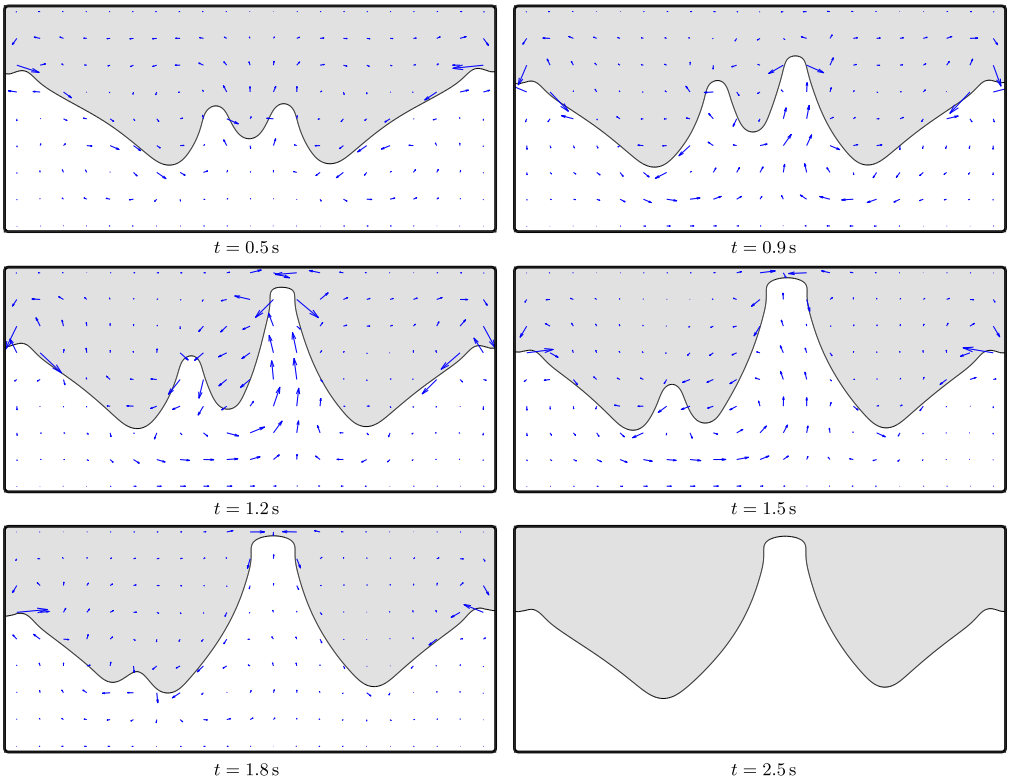

FIG. 9. Time evolution (averaged over one excitation period) of the frozen wave instability with $g = 0.5g_0$ in a container of size $L \times 2H = 30 \times 15$ mm vibrated at $f = 45$ Hz with $A = 1.6$ mm ($v = 0.452$ m/s, $\mathcal{F} = 15.06$). A mode transition between the $\mathcal{K} = 3$ and $\mathcal{K} = 2$ patterns is observed. The snapshot times are labeled and the mean velocity field during the transient period is shown using scaled arrows (scale differs between snapshots). For $t \lesssim 0.5$ s the evolution is similar to that of Fig. 8(b).

The experiments of Shevtsova *et al.* [11] with miscible liquids and those of Salgado Sánchez *et al.* [12] with immiscible liquids both showed that, in microgravity, the finite container depth is what limits wave growth in moderately sized containers. Initially sinusoidal frozen wave perturbations grow quickly into large columnar structures stretching between the lower and upper boundaries. The threshold for observing these patterns is extremely low in microgravity and vanishes in the ideal limit of an infinitely long container with $g = 0$, as seen from Eq. (11). It is the finite container length that determines the minimum wave number and, thus, the threshold for instability [8].

This theoretical threshold, however, is modified by the vibroequilibria effect, which is magnified in microgravity and belies the assumption of an underlying flat interface. The effect is proportional to v^2 and has no threshold [14,30] so, prior to the frozen wave instability, the average interface profile is that of the symmetric vibroequilibria state [29]. The amplitude of this state is characterized in Fig. 10(a) by the difference Δh between the height of the contact points and the interface at the midpoint of the container. This figure confirms the predicted quadratic dependence: $\Delta h \propto v^2$. Furthermore, the vibroequilibria solutions are in good agreement with the theoretical results of Fernández *et al.* [29] and the microgravity experiments of Salgado Sánchez *et al.* [32].

Although the vibroequilibria state qualitatively resembles the $\mathcal{K} = 1$ frozen wave mode, one can still locate an instability threshold separating continuous vibroequilibria growth from the rapid formation of a columnar pattern like that shown in the inset of Fig. 10(b). As noted earlier, the

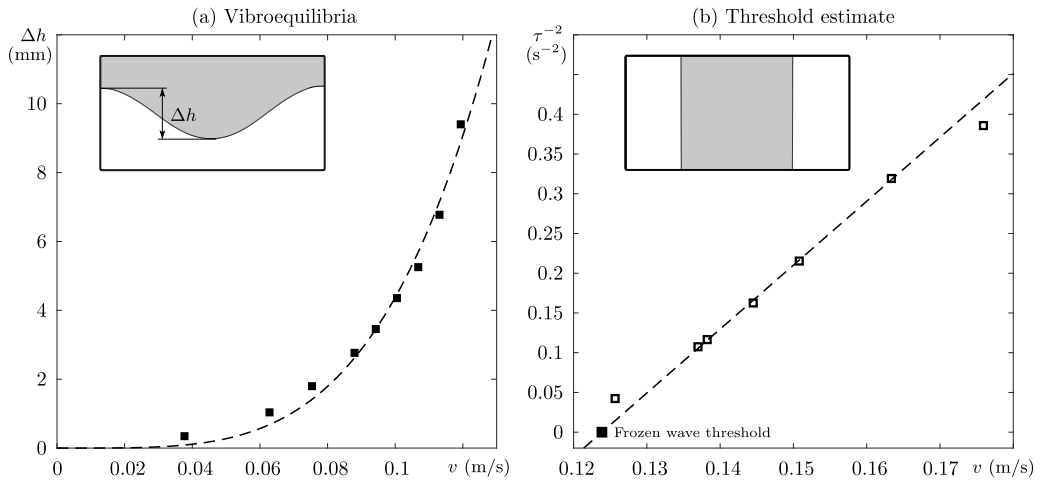

FIG. 10. (a) Evolution of the symmetric vibroequilibria state in microgravity with increasing velocity v in a container of size $L \times 2H = 30 \times 15$ mm. The difference Δh between the height of the contact points and the midpoint of the interface is shown and fitted (dashed line) to a quadratic function as per the theoretical prediction. The inset illustrates a typical vibroequilibria state and the Δh measurement. (b) Inverse square of the frozen wave growth time, τ^{-2} (open squares), for the smallest wave number $\mathcal{K} = 1$ versus v. The observed linear dependence allows for an estimation of the instability threshold (black marker). The inset shows the final columnar pattern resulting from the $\mathcal{K} = 1$ mode.

preexisting vibroequilibria state strongly favors a frozen wave (columnar) solution with the heavier liquid along the sides and (for $\mathcal{K} = 1$) a doubly wide region of lighter liquid in the interior. We note that this final configuration can also develop directly from the symmetric vibroequilibria state if the amplitude reaches $\Delta h \simeq 2H$.

To locate the frozen wave threshold for $g = 0$, we follow Ref. [8] and measure the transient time τ required for the interface at the central trough to reach the bottom of the container. For stable vibroequilibria states, τ is infinite, while it decreases beyond the frozen wave threshold. From the observation that τ^{-2} is nearly linear in v and the assumption that the frozen wave instability is either subcritical or nearly degenerate (i.e., there is no significant interval of bounded frozen waves with $\Delta h < 2H$), one can estimate the threshold v_c from the intercept of a simple linear fit. The measured (inverse square) growth times are shown in Fig. 10(b) (open squares) along with the linear fit (dashed line) and the estimated threshold (solid square) at $v_c \simeq 0.124$ m/s.

V. EFFECT OF BOND NUMBER

Figure 11 summarizes the results of a systematic series of numerical simulations with gravity levels (in units of g_0) of 0.25, 0.5, 0.75, 1, 1.5, and 2. The same analysis and fitting procedure is performed at each g value to construct Fig. 12, which shows the dependence on Bond number (Bo) of the critical amplitude $\mathcal{F}_c$, the transition value $\mathcal{F}^*$ that marks the beginning of the gravity regime, and the remaining fitting parameters expressed in dimensionless form (denoted by a hat),

$$(\widehat{K}, \widehat{\mathcal{M}}) = \sqrt{\frac{\sigma}{(\rho_1 - \rho_2)H^3}}\,(K, \mathcal{M}), \quad \widehat{\epsilon} = \frac{\epsilon}{H^3}. \tag{28}$$

In Figs. 12(a) and 12(b), the fitting parameters obtained with $\widehat{\epsilon} = 0$ are shown with open circles, while those obtained with the $\widehat{\epsilon} \neq 0$ values of Fig. 12(d) are shown with crosses; the values often overlap.

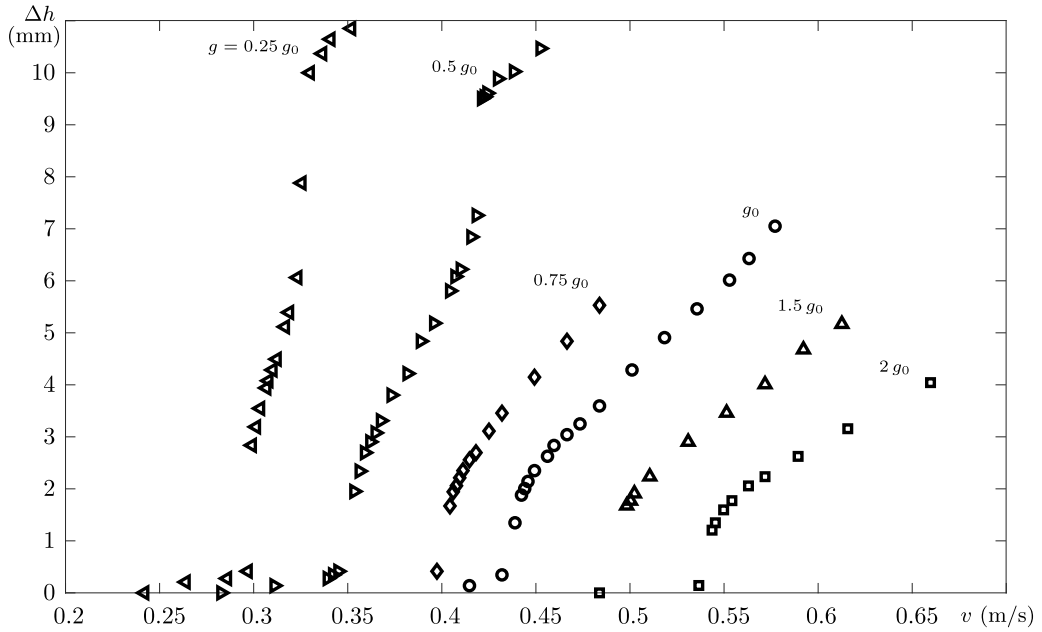

FIG. 11. Bifurcation diagrams obtained for the $L \times 2H = 30 \times 15$ mm container with varying gravity levels (in units of g_0): 0.25, 0.5, 0.75, 1, 1.5, 2. The data sets are distinguished with different markers and labeled with the gravity level used. Note that for $g = 0.25g_0$ and $0.5g_0$, the finite-depth regime discussed in Sec. IV B is visible at large amplitude.

From the results summarized in these figures, the following conclusions about the influence of gravity may be drawn.

(i) The frozen wave threshold $\mathcal{F}_c$ decreases with decreasing Bo until reaching a minimum value determined by the longest wavelength allowed in the container [8].

(ii) The branching coefficient $\widehat{K}$ of the capillary-gravity regime grows with decreasing Bo and appears to diverge as $\mathrm{Bo} \to 0$.

(iii) The slope $\widehat{\mathcal{M}}$ of the approximately linear growth in the gravity regime similarly grows with decreasing Bo and appears to diverge as $\mathrm{Bo} \to 0$.

The apparent divergence of $\widehat{K}$ and $\widehat{\mathcal{M}}$ with decreasing Bo reflects the crucial role of gravity as a restoring force for frozen waves. Gravity dominates for large-amplitude waves and is commensurate with interfacial tension near onset. Since the scale of the frozen wave instability in an infinitely deep and extended system is set by the capillary length l_c, both gravitational and interfacial restoring forces are in balance near onset and decrease together with decreasing Bo (see Sec. III B). For $\mathrm{Bo} = 0$, there is no restoring force at all and the pitchfork bifurcation is degenerate ($\widehat{K} = \infty$). This argument, however, does not hold for finite containers since there is a minimum allowed wave number, which arrests the declining influence of interfacial tension. For large enough σ in a container of finite length, it should be possible to observe small-amplitude frozen waves even with $\mathrm{Bo} = 0$. Such small-amplitude frozen waves were not seen with the parameters of Table I, suggesting that for realistic liquids in containers of the size used here, or larger, the (perturbed) pitchfork bifurcation to frozen waves with $g = 0$ is, effectively, degenerate. The same conclusion can be inferred directly from the tendency of the bifurcation diagrams in Fig. 11.

A. Comparison with theory

The expression (12) derived by Lyubimov and Cherepanov [5] can be compared with the critical forcing $\mathcal{F}_c$ obtained from the fitting procedure. Since the wave number here is limited by the length

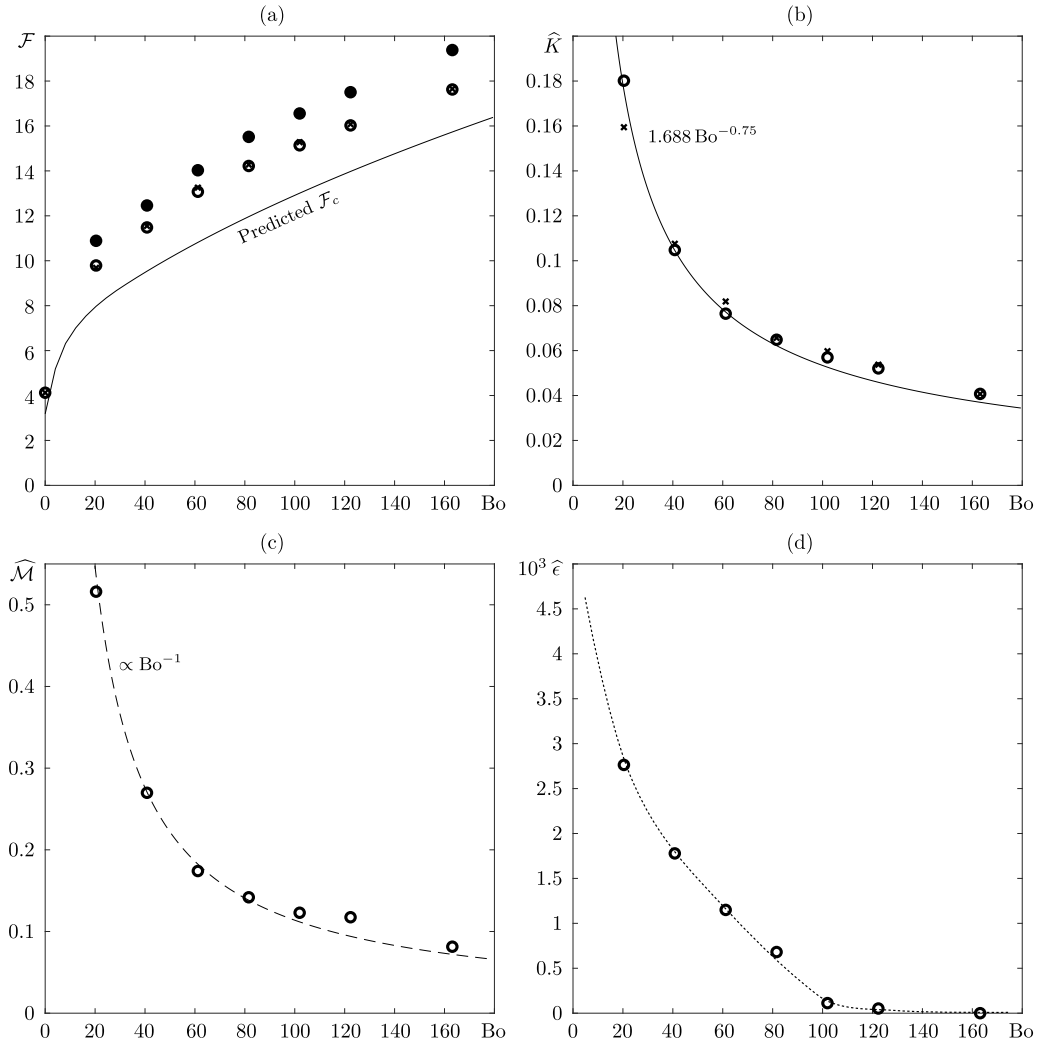

FIG. 12. Dimensionless fitting parameters characterizing the frozen wave bifurcation diagram as a function of the Bond number Bo: (a) critical forcing $\mathcal{F}_c$ (open circles for $\widehat{\epsilon} = 0$, crosses for $\widehat{\epsilon} \neq 0$) and the point of transition to the gravity regime $\mathcal{F}^*$ (solid circles), (b) branching coefficient $\widehat{K}$ of the gravity-capillary regime (open circles for $\widehat{\epsilon} = 0$, crosses for $\widehat{\epsilon} \neq 0$), (c) slope $\widehat{\mathcal{M}}$ of the gravity regime, and (d) symmetry-breaking parameter $\widehat{\epsilon}$. The predicted value for $\mathcal{F}_c$ from Eq. (12) is shown with a solid curve in (a) while the theoretical formula for $\widehat{K}$ from Eq. (16) is shown in (b). The dashed curve in (c) shows a fit to Bo^{-1} while the dotted curve in (d) is intended only as a visual aid. The values of $\mathcal{F}^*$ and $\widehat{\mathcal{M}}$ change imperceptibly between the $\widehat{\epsilon} = 0$ and $\widehat{\epsilon} \neq 0$ cases.

L, we minimize Eq. (12) over wave numbers between $k_{\min} = 2\pi/L$ and $k_{\max} \approx 7\pi/L$, which is the maximum observed in the simulations. This prediction is shown in Fig. 12(a) with a solid curve. Note that the measured threshold values are in good agreement with the dependence of the theoretical curve, except for a delay of approximately 20%. This shift is likely due to a combination of the vibroequilibria effect, other finite-size effects, and viscosity. In fact, the viscosity contrast used here, $\widehat{\nu} = 20$, lies in a range shown by Talib *et al.* [6] to delay the onset of frozen waves compared to the prediction of the inviscid linear theory.

The branching coefficient $\widehat{K}$ in the case of an infinitely deep extended system is that of Eq. (16):

$$\widehat{K} = \sqrt{\frac{16(1-\widehat{\rho}^{\,2})}{\widehat{\rho}\,(42\,\widehat{\rho} - 11 - 11\,\widehat{\rho}^{\,2})}}\,\mathrm{Bo}^{-3/4} \simeq 1.688\,\mathrm{Bo}^{-3/4}. \tag{29}$$

This expression is evaluated for $\widehat{\rho} = 0.52$, which is the density ratio for 100 cSt silicone oil and FC-40, and is shown as a solid curve in Fig. 12(b). The agreement of the fitting coefficient with Eq. (29) is excellent, despite the fact that wave number selection in the simulations is complicated by vibroequilibria and finite-size effects. The level of agreement further suggests that viscosity does not significantly affect the weakly nonlinear frozen wave growth.

B. Symmetry-breaking due to vibroequilibria

The symmetry-breaking effect of vibroequilibria is quantified by the parameter $\widehat{\epsilon}$. Figure 12(d) shows the values obtained with Bond numbers corresponding to $g = 0.25,\ 0.5,\ 0.75\,,\ 1,\ 1.25,\ 1.5,\ 2\,g_0$. As expected from the flattening effect of gravity on the interface, $\widehat{\epsilon}$ decreases with increasing Bond number. Strong gravity masks the preference for solutions with heavier fluid along the lateral walls, and the bifurcation diagram more closely resembles an ideal supercritical pitchfork.

VI. CONCLUSIONS

The influence of gravity on the frozen wave instability induced by periodic horizontal excitation was investigated with extensive numerically simulations modeling two immiscible fluids with properties characteristic of FC-40 and 100 cSt silicone oil, which are relevant to recent microgravity [12,18] and ground [17] experiments. The simulations were begun from an initially flat interface separating liquids of equal volume, used gravity levels from 0 to $2g_0$, and (most) were performed in a 30×15 mm rectangular domain. The dynamics were resolved using a standard level-set formulation by means of the finite-element method, as described in Sec. II.

The evolution of the interface following the frozen wave instability was considered under terrestrial and hypergravity conditions in Sec. III and characterized by the trough-to-crest distance for different applied velocities. The resulting diagram shows that frozen waves emerge via a perturbed (asymmetric) supercritical pitchfork bifurcation. The symmetry breaking is attributed to the vibroequilibria effect, which promotes a fluid distribution with the heavier fluid displaced upward along the lateral walls. Near onset, wave amplitude varies as the square root of the applied velocity difference, consistent with the prediction of inviscid theory in infinitely deep, extended systems [5]. The threshold and branching coefficients are determined from least-squares fits, as described in Sec. III B. The interface often exhibits an inverted trochoid-like shape, in agreement with the experiments of Jalikop and Juel [17].

As the forcing is raised further above onset, a transition is observed wherein the frozen waves adopt a more finger-like profile and the amplitude grows nearly linearly with applied velocity. This transition is also evident from the radius of curvature [17] at the crests, which near this point reaches an asymptotic value comparable to the capillary length. As the shape of the tips (crests) remains nearly constant, an increase in forcing (equivalently, wave amplitude) is counteracted primarily by gravity, with interfacial energy playing a diminishing role. This is in contrast to the situation near onset, where interfacial and gravitational forces are of similar magnitude.

The frozen wave instability in reduced gravity is considered in Sec. IV. As anticipated from the ideal linear theory [5], the threshold is lowered. Furthermore, beyond the transition from the initial gravity-capillary (square-root) regime to the gravity-dominated (linear) regime, a third type of behavior is found when the wave amplitude becomes comparable to the container depth. The growth of the crests is bounded in this regime by the upper wall of the container, while the troughs remain a certain distance from the bottom; this is reflected in the bifurcation diagram as a kind of amplitude saturation. In the limit of zero gravity, the frozen waves rapidly develop into a series

of alternating columns spanning the container height. The threshold, although low, remains finite in containers of finite length, since there is a minimum allowed wave number, and is calculated following the method of Ref. [8].

The results of all simulations are summarized through the parameters defining the bifurcation diagram, shown as a function of Bond number (Bo) in Sec. V. The threshold is compared with the prediction of the ideal linear theory and the branching coefficient with the prediction of the corresponding weakly nonlinear theory [5]. Qualitative agreement is obtained for the threshold, which is delayed due to viscosity [6], vibroequilibria, and finite-size effects [8]. Excellent agreement is obtained for the branching (nonlinear) coefficient despite the complicated wave number selection occurring in this system, suggesting as well that viscosity does not significantly affect the nonlinear frozen wave growth, at least near onset. Since both coefficients relating wave amplitude to forcing appear to diverge as $\mathrm{Bo} \to 0$, the (perturbed) pitchfork bifurcation can be considered to be effectively degenerate for $g = 0$. However, because the symmetry-breaking effect of vibroequilibria is magnified in this limit, there is no "true" bifurcation but, rather, a continuous transition from a vibroequilibria to a frozen wave solution. Despite this fact, the suddenness of the (nearly degenerate) transition allows a threshold to be located with reasonable accuracy. In the large Bond number limit, on the other hand, the vibroequilibria effect is reduced and the bifurcation approaches the predicted supercritical pitchfork.

ACKNOWLEDGMENTS

The work of D.G., P.S.S., and J.P. was supported by the Ministerio de Economía y Competitividad under Project No. ESP2015-70458-P. The work of V.S. was supported by the PRODEX program of the Belgian Federal Science Policy Office. We also thank A. Nepomnyaschy for helpful discussions.

[1] H. Kull, Theory of the Rayleigh-Taylor instability, Phys. Rep. **206**, 197 (1991).
[2] G. K. Batchelor, Heat convection and buoyancy effects in fluids, Q. J. R. Meteorol. Soc. **80**, 339 (1954).
[3] R. V. Birikh, Thermocapillary convection in a horizontal layer of liquid, J. Appl. Mech. Tech. Phys. **7**, 43 (1966).
[4] G. H. Wolf, The dynamic stabilization of the Rayleigh-Taylor instability and the corresponding dynamic equilibrium, Z. Phys. **227**, 291 (1969).
[5] D. V. Lyubimov and A. A. Cherepanov, Development of a steady relief at the interface of fluids in a vibrational field, Fluid Dyn. **21**, 849 (1986).
[6] E. Talib, S. V. Jalikop, and A. Juel, The influence of viscosity on the frozen wave stability: Theory and experiment, J. Fluid Mech. **584**, 45 (2007).
[7] T. P. Lyubimova, A. O. Ivantsov, Y. Garrabos, C. Lecoutre, G. Gandikota, and D. Beysens, Band instability in near-critical fluids subjected to vibration under weightlessness, Phys. Rev. E **95**, 013105 (2017).
[8] P. Salgado Sánchez, Y. A. Gaponenko, J. Porter, and V. Shevtsova, Finite-size effects on pattern selection in immiscible fluids subjected to horizontal vibrations in weightlessness, Phys. Rev. E **99**, 042803 (2019).
[9] Y. A. Gaponenko, M. M. Torregrosa, V. Yasnou, A. Mialdun, and V. Shevtsova, Interfacial pattern selection in miscible liquids under vibration, Soft Matter **11**, 8221 (2015).
[10] Y. A. Gaponenko, A. Mialdun, and V. Shevtsova, Pattern selection in miscible liquids under periodic excitation in microgravity: Effect of interface width, Phys. Fluids **30**, 62103 (2018).
[11] V. Shevtsova, Y. A. Gaponenko, V. Yasnou, A. Mialdun, and A. Nepomnyashchy, Two-scale wave patterns on a periodically excited miscible liquid-liquid interface, J. Fluid Mech. **795**, 409 (2016).
[12] P. Salgado Sánchez, V. Yasnou, Y. Gaponenko, A. Mialdun, J. Porter, and V. Shevtsova, Interfacial phenomena in immiscible liquids subjected to vibrations in microgravity, J. Fluid Mech. **865**, 850 (2019).
[13] T. Lyubimova, A. Ivantsov, Y. Garrabos, C. Lecoutre, and D. Beysens, Faraday waves on band pattern under zero gravity conditions, Phys. Rev. Fluids **4**, 064001 (2019).

[14] D. V. Lyubimov, A. A. Cherepanov, T. P. Lyubimova, and B. Roux, Interface orienting by vibration, C. R. Acad. Sci. - Series IIB - Mechanics-Physics-Chemistry-Astronomy **325**, 391 (1997).
[15] K. Beyer, I. Gawriljuk, M. Günther, I. Lukovsky, and A. Timokha, Compressible potential flows with free boundaries. Part I: Vibrocapillary equilibria, Z. Angew. Math. Mech. **81**, 261 (2001).
[16] M. Faraday, On a peculiar class of acoustical figures; and on certain forms assumed by groups of particles upon vibrating elastic surfaces, Philos. Trans. R. Soc. London **121**, 299 (1831).
[17] S. V. Jalikop and A. Juel, Steep capillary-gravity waves in oscillatory shear-driven flows, J. Fluid Mech. **640**, 131 (2009).
[18] P. Salgado Sánchez, Y. Gaponenko, V. Yasnou, A. Mialdun, J. Porter, and V. Shevtsova, Effect of initial interface orientation on patterns produced by vibrational forcing in microgravity, J. Fluid Mech. **884**, A38 (2020).
[19] E. Olsson and G. Kreiss, A conservative level set method for two phase flow, J. Comput. Phys. **210**, 225 (2005).
[20] D. B. Kothe, R. C. Mjolsness, and M. D. Torrey, RIPPLE: A Computer Program for Incompressible Flows with Free Surfaces, Tech. Rep. LA-12007-MS (Los Alamos National Laboratory, 1991).
[21] S. Someya and T. Munakata, Measurement of the interface tension of immiscible liquids interface, J. Cryst. Growth **275**, 343 (2005).
[22] S. Erlicher, L. Bonaventura, and O. Bursi, The analysis of the generalized-α method for non-linear dynamic problems, Comput. Mech. **28**, 83 (2002).
[23] I. Harari and T. J. Hughes, What are C and h?: Inequalities for the analysis and design of finite element methods, Comput. Methods Appl. Mech. Eng. **97**, 157 (1992).
[24] R. Codina, A discontinuity-capturing crosswind-dissipation for the finite element solution of the convection-diffusion equation, Comput. Methods Appl. Mech. Eng. **110**, 325 (1993).
[25] G. Gandikota, D. Chatain, S. Amiroudine, T. Lyubimova, and D. Beysens, Frozen-wave instability in near-critical hydrogen subjected to horizontal vibration under various gravity fields, Phys. Rev. E **89**, 012309 (2014).
[26] F. Varas and J. M. Vega, Modulated surface waves in large-aspect-ratio horizontally vibrated containers, J. Fluid Mech. **579**, 271 (2007).
[27] I. Tinao, J. Porter, A. Laveron-Simavilla, and J. Fernández, Cross-waves excited by distributed forcing in the gravity-capillary regime, Phys. Fluids **26**, 024111 (2014).
[28] P. Salgado Sánchez, J. Porter, I. Tinao, and A. Laverón-Simavilla, Dynamics of weakly coupled parametrically forced oscillators, Phys. Rev. E **94**, 022216 (2016).
[29] J. Fernández, I. Tinao, J. Porter, and A. Laveron-Simavilla, Instabilities of vibroequilibria in rectangular containers, Phys. Fluids **29**, 024108 (2017).
[30] I. Gavrilyuk, I. Lukovsky, and A. Timokha, Two-dimensional variational vibroequilibria and Faraday's drops, Z. Angew. Math. Phys. **55**, 1015 (2004).
[31] J. Fernández, P. Salgado Sanchez, I. Tinao, J. Porter, and J. M. Ezquerro, The CFVib experiment: Control of fluids in microgravity with vibrations, Microgravity Sci. Technol. **29**, 351 (2017).
[32] P. Salgado Sánchez, J. Fernández, I. Tinao, and J. Porter, Vibroequilibria in microgravity: Comparison of experiments and theory, Phys. Rev. E **100**, 063103 (2019).
[33] S. Strogatz, *Nonlinear Dynamics and Chaos: With applications to Physics, Biology, Chemistry, and Engineering* (CRC Press, Boca Raton, FL, 1994).
[34] Y. A. Gaponenko, M. M. Torregrosa, V. Yasnou, A. Mialdun, and V. Shevtsova, Dynamics of the interface between miscible liquids subjected to horizontal vibration, J. Fluid Mech. **784**, 342 (2015).
[35] Y. A. Gaponenko and V. Shevtsova, Shape of the diffusive interface under periodic excitations at different gravity levels, Microgravity Sci. Technol. **28**, 431 (2016).
[36] D. V. Lyubimov, A. O. Ivantsov, T. P. Lyubimova, and G. L. Khilko, Numerical modeling of frozen wave instability in fluids with high viscosity contrast, Fluid Dyn. Res. **48**, 061415 (2016).
[37] A. V. Burnysheva, D. V. Lyubimov, and T. P. Lyubimova, Disturbance spectrum of a plane fluid-fluid interface in the field of tangential high-frequency vibrations underweightlessness, Fluid Dyn. **46**, 1000 (2011).